metals

MDPI

Article

Investigating the Static Recrystallization Behavior of 22MnB5 Manganese–Boron Steel through Stress Relaxation Analysis

Peter Birnbaum [1,*], Stefan Pilz [2], Kai Neufeld [2] and Andreas Kunke [1]

[1] Institute for Machine Tools and Production Processes (IWP), Chemnitz University of Technology, 09107 Chemnitz, Germany; uff@tu-chemnitz.de
[2] Institute for Materials Chemistry (IMC), Leibniz-Institute for Solid State and Materials Research Dresden, 01069 Dresden, Germany; s.pilz@ifw-dresden.de (S.P.); k.neufeld@ifw-dresden.de (K.N.)
* Correspondence: peter.birnbaum@mb.tu-chemnitz.de

Abstract: A constitutive model was developed to characterize the static recrystallization (SRX) and evolution of the grain size of the industrially relevant press-hardening steel, 22MnB5, subsequent to the hot forming of sheet metal. Isothermal stress relaxation tests were conducted using the BAEHR 805 A/D thermomechanical simulator, encompassing a temperature range of 950 to 1050 °C, prestrain levels ranging from 0.01 to 0.1, and strain rates spanning from 0.01 to 0.8 s^{-1}. The results obtained from the isothermal stress relaxation tests facilitated the formulation of an Avrami equation-based model, which aptly describes the kinetics of SRX in relation to the temperature, prestrain, and strain rate. Notably, an increase in temperature led to accelerated recrystallization kinetics, signifying temperature-dependent behavior. When the temperature increased from 950 to 1050 °C, the recrystallization time was reduced to approximately one-third. Additionally, the prestrain exhibited a positive influence on the acceleration of SRX kinetics. A quintupling of the prestrain from 0.01 to 0.05 resulted in a reduction of the static recrystallization duration to approximately one-fifth. Among the parameters studied, the strain rate had the least impact on the SRX kinetics, as doubling the strain rate from 0.01 to 0.8 only resulted in a halving of the recrystallization duration. Moreover, an analysis of the microstructural evolution in response to the forming parameters was undertaken. While the grain-size investigation post-isothermal stress relaxation tests provided results in line with the SRX kinetics calculations, the observed effects were comparatively subdued. Furthermore, a comprehensive examination was conducted using electron backscatter diffraction (EBSD) analysis, aiming to explore the effects of specific stress relaxation states on the morphology of martensite. The findings reveal fully recrystallized globulitic microstructures, characterized by relatively minor differences among them.

Keywords: constitutive model; static recrystallization; martensite morphology; 22MnB5; EBSD

Citation: Birnbaum, P.; Pilz, S.; Neufeld, K.; Kunke, A. Investigating the Static Recrystallization Behavior of 22MnB5 Manganese–Boron Steel through Stress Relaxation Analysis. *Metals* **2023**, *13*, 1646. https://doi.org/10.3390/met13101646

Academic Editor: Talal Al-Samman

Received: 14 August 2023
Revised: 18 September 2023
Accepted: 18 September 2023
Published: 25 September 2023

1. Introduction

The low-alloyed steel 22MnB5 is widely utilized in the car manufacturing industry for its high-strength properties, making it a preferred material for structural components, such as B-pillars and anti-collision beams [1,2]. The desired high strength of these components is achieved through a hot stamping process [3–5], wherein the steel is heated above its austenitization temperature and subsequently formed in a cooled die. During this interaction with the cooled tool, the rapid cooling of the 22MnB5 sheet triggers a martensitic transformation within its microstructure, leading to a significant increase in the steel hardness. During the deformation of austenite at high temperatures, both hardening and softening mechanisms operate concurrently, significantly impacting the stamp load and microstructure evolution. Hardening primarily results from work hardening during forming, while softening is attributed to the recrystallization of austenite. The recrystallization process involves dynamic recrystallization (DRX) and so-called static recrystallization

(SRX) [6]. When the strain imposed remains below the critical threshold for DRX, and the deformed sheets are maintained at elevated temperatures, SRX becomes the dominant recrystallization mechanism [7]. Understanding the SRX behavior of austenite during hot stamping is crucial, requiring the establishment of an SRX kinetics model to study the softening mechanism. Currently, the conventional approach to investigating the SRX behavior of austenite involves calculating the true stress–strain curve obtained through two or more passes of hot compression deformation, utilizing the offset method [8,9]. This method determines the yield strength corresponding to a strain offset of either 0.2% or 2%. Several researchers have employed the offset method or the so-called double compression test to assess the SRX behavior of low-alloyed steel. Their findings have consistently indicated that the softening caused by SRX is promoted with increasing deformation temperature and strain [10–12]. Zhao et al. [13] further explored the SRX behavior of 300 M steel using high-temperature laser scanning confocal microscopy. They extensively discussed the flow behavior variations and microstructure under various deformation conditions, identifying the primary SRX mechanism as strain-induced boundary migration. In a separate study, Luo et al. [14] investigated the SRX behavior of Z12CN13 martensite stainless steel through double compression tests. Their research revealed that the main nucleation mechanism was bulging at grain boundaries, while undissolved precipitates, such as $MoNi_3$ and Fe_3C, retarded the recrystallization kinetics. Additionally, Wang et al. [15] delved into the SRX mechanism of ultrahigh-strength stainless steel (UHSS) with the help of double compression tests. Their findings highlighted the effect of deformation conditions and initial microstructures on SRX kinetics and microstructural evolution, alongside a suppression of SRX due to the pinned effect of carbide precipitation on boundaries below 1050 °C. Kaikkonen et al. [16] successfully adapted the equation according to Boratto in order to determine the non-recrystallization temperature, investigating the effect of molybdenum content and increased silicon concentrations of medium carbon bainitic steels. Through alloying with Mo and microalloying elements, such as Ti, V, and Nb [17], it has been demonstrated that the SRX process is effectively impeded and shifted to higher temperatures. Facusseh et al. [18] conducted stepwise and continuous hot forming tests on eutectoid steel within a temperature range from 850 °C to 1050 °C. Their results indicated that an increase in carbon content accelerated the SRX rate.

The novelty of this publication lies in the examination of static recrystallization for 22MnB5 within the process window of the hot stamping process to enhance the prediction of component properties. Stress relaxation tests (SRT) were employed to determine the SRX mechanism of 22MnB5 within the hot stamping temperature window of 950–1050 °C. The utilization of SRT offers several advantages, including substantially reduced experimental specimen requirements and the efficient calculation of both the recovery and recrystallization kinetics of hot-worked austenite, in contrast to the double compression test [19]. The impact of the deformation temperature, the strain rate, and the prestrain on the SRX behavior of 22MnB5 are thoroughly discussed. Additionally, the influence of SRX grains on the martensite morphology that is formed after stress relaxation and subsequent quenching is further analyzed using electron backscatter diffraction (EBSD) analysis to describe the evolution of the parental austenite grain boundary, packets, and blocks. The parameterized model enables integration into finite element (FE) software, enabling the prediction of the statically recrystallized fraction and the predominant grain size. Consequently, ideal temperatures and forming parameters can be calculated to selectively adjust component properties.

2. Experimental Procedure

The material utilized in this study was 22MnB5 commercial boron steel, with the chemical composition (wt.%) detailed in Table 1.

Table 1. Chemical composition of investigated 22MnB5 alloy, balance Fe (wt %).

C	Si	Mn	P	S	Al	Ti	Nb
0.2028	0.3712	1.162	0.0135	0.00196	0.05718	0.0325	0.00308
B	**Cr**	**Cu**	**Mo**	**Ni**	**Ta**	**W**	**V**
0.00146	0.2688	0.0301	0.03936	0.05882	0.00736	0.005	0.0045

The normalized 22MnB5 steel exhibited an initial microstructure comprising equiaxial ferrite and globulitic pearlite, as illustrated in Figure 1. For experimentation purposes, cylindrical specimens were machined from a 9 mm thick plate, with their longitudinal axis aligned in the rolling direction. The specimens' dimension was 5 mm in diameter and 10 mm in height. To delve into the process of SRX, stress relaxation tests were conducted using the BAEHR 805 A/D thermo-mechanical simulator. The experimental setup is depicted in Figure 2.

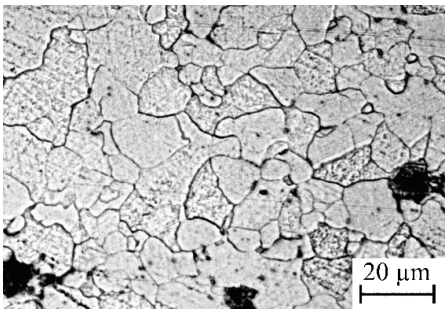

Figure 1. Initial microstructure of as-received 22MnB5 steel.

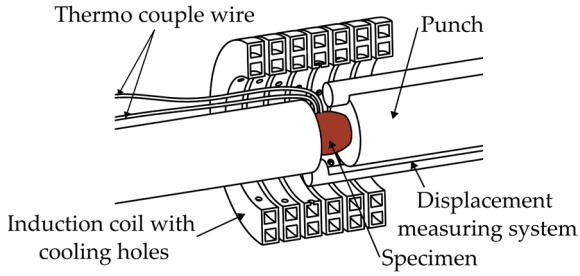

Figure 2. Sketch of experimental setup for thermo-mechanical simulation.

The specimens were subjected to a heat treatment process to obtain full austenization at a temperature of 950 °C under vacuum conditions, with a heating rate of 3 K/s, and they were held at this temperature for a duration of 300 s. Subsequently, a rapid heating rate of 25 K/s was applied to eliminate temperature gradients, and the specimens were maintained at the deformation temperature for 15 s. Following pre-compression at specific strain and temperature levels, the specimens were fixed using clamping anvils. Concurrently, force relaxation measurements were performed to assess the softening effect. The stress relaxation tests (SRT) were carried out within the hot stamping forming window of the austenized workpieces. This encompassed three relaxation temperatures of 950, 1000, and 1050 °C, three different strain rates of 0.01, 0.1, and 0.8 s^{-1}, and four distinct prestrains (0.01, 0.03, 0.05, and 0.1), as outlined in the schedule illustrated in Figure 3. Afterward, the relaxed specimens underwent quenching with argon under high pressure to ensure complete martensite transformation. All specimens were sectioned along the axial plane and subsequently etched using a picric acid solution (comprising 280 mL of deionized water, 5.5 g of picric acid, 2 mL of hydrochloric acid, and 8.4 mL of Teepol) to reveal the former austenite grain boundaries. The microstructure was then meticulously examined using a Zeiss Axio Vert. A1 MAT, and the average grain size was determined through the intercept method [20]. Finally, electron backscatter diffraction (EBSD) studies were

conducted using a Zeiss Gemini 1530 FEG-SEM equipped with an EBSD detector (Bruker e-FlashHR, Billerica, MA, USA) to analyze the martensite microstructure. Grain maps were generated with a minimum grain boundary threshold of 3° using the MTEX (version 5.1.1) free texture and crystallography analysis toolbox. By use of an algorithm developed by Nyyssönen et al. [21], the parent austenite grain (PAG) and the packet and block boundaries of the predominant martensite were calculated.

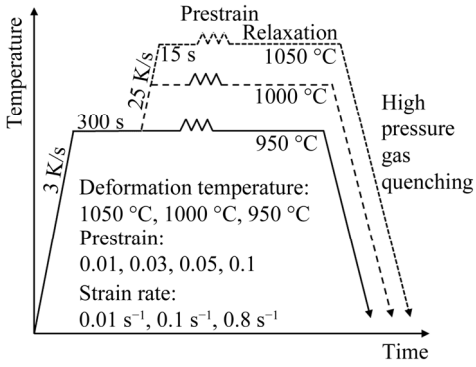

Figure 3. Experimental procedure for stress relaxation tests.

The stress relaxation curve of carbon steel exhibits three distinct stages, as depicted in Figure 4, as observed in previous studies [19]. In the first and third stages, the relationship between true stress and logarithmic time is nearly linear. During the initial stage, true stress displays a gradual decrease with a constant rate, attributed to the creep and recovery of deformed austenite. The second stage corresponds to the actual SRX process, which demonstrates a considerably more pronounced softening effect than the first stage. In the third stage, a second linear relationship with a slow stress decrease is observed, indicative of the completion of SRX and the onset of new grain growth. The observed behavior can be effectively described using the model proposed by Karjalainen et al. [22], which is outlined as follows:

$$X_{srx} = \frac{\sigma_1 - \alpha_1 \cdot \log(t) - \sigma}{(\sigma_1 - \sigma_2) - (\alpha_1 - \alpha_2) \cdot \log(t)} \quad (1)$$

$$\sigma = \sigma_1 - \alpha_1 lg(t) \quad (2)$$

$$\sigma = \sigma_2 - \alpha_2 lg(t) \quad (3)$$

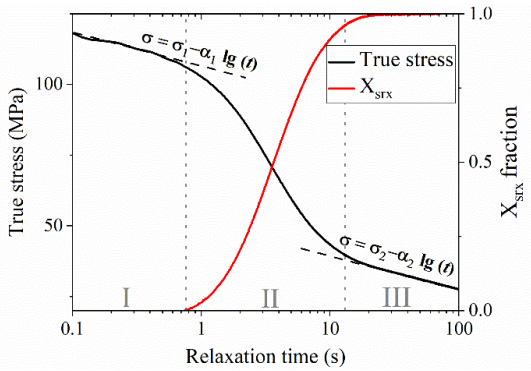

Figure 4. Typical relaxation stress–time curve, with recovery stage (no. I), post-deformation stage of recrystallization (no. II), and grain growth stage (no. III) [19].

In Equation (1), σ represents the true stress, $\sigma_{1,2}$ and $\alpha_{1,2}$ are material constants, and t denotes the relaxation time after deformation. Equations (2) and (3) are employed to characterize the stress behavior during the first and third stages, respectively. Notably,

during the second stage, an abrupt drop in stress occurs due to the pronounced softening effect resulting from SRX. Assuming that the material consists solely of work-hardened austenite and fully softened austenite during this stage, the stress σ in the recrystallization phase is expressed as a function of the relaxation time t, given by:

$$\sigma = (1 - X)(\sigma_1 - \alpha_1 \lg(t)) + X(\sigma_2 - \alpha_2 \lg(t)) \quad (4)$$

where X is the fraction of softened material. As a function of time, SRX can be expressed by the Avrami equation [22]:

$$X = 1 - \exp[X_1 \left(\frac{t}{t_{0.5}} \right)^{X_2}] \quad (5)$$

where $t_{0.5}$ is the required time for 50% of recrystallization, and X_1, X_2 are the SRX constants of Equation (5). The parameter $t_{0.5}$ is affected by several factors, including the deformation temperature [22,23], plastic strain, strain rate, and the initial austenite grain size, and can be expressed by Equation (6):

$$t_{0.5} = T_{s1} \varepsilon^{T_{s2}} \dot{\varepsilon}^{T_{s3}} \exp(\frac{Q_{Ts}}{RT}) \quad (6)$$

T_{s1}, T_{s2}, and T_{s3} are the material-related constants in Equation (6), ε is the amount of prestrain, $\dot{\varepsilon}$ is the strain rate, T is the deformation temperature, Q_{Ts} is the activation energy for SRX, and the parameter R is the universal gas constant. The corresponding values for T_{s1}, T_{s2}, T_{s3}, Q_{Ts}, X_1, and X_2 can be obtained as described in Section 3.3.

3. Results and Discussion

3.1. Stress Relaxation Curves

A representative set of stress relaxation curves was generated under different deformation conditions for 22MnB5, as shown in Figure 5. Notably, all curves exhibited three distinct stages, as previously observed (see Figure 4), with an increasing relaxation time. In Figure 5a, the effect of temperature on SRX is illustrated. It is evident that as the temperature rose, the yield stress decreased, with the relaxation curve for 1050 °C exhibiting the lowest yield stress. At 1050 °C, the recovery process was the shortest, and recrystallization started the earliest. Higher temperatures provided a greater driving force for SRX, given its diffusion-controlled nature. Figure 5b showcases the impact of prestrain on the recovery phase (phase I as per Figure 4). A prestrain of 0.05 resulted in the highest yield stress during the recovery phase. This is attributed to the substantial generation of dislocations during hot forming, leading to an increase in dislocation density. Dislocations significantly contributed to strain hardening by hindering further dislocation movement, thereby enhancing the material strength and elevating the yield stress during the forming process. Higher prestrains, such as 0.05, generated more dislocations and subsequently yielded larger yield stresses compared to the prestrains of 0.01 and 0.03 at a constant strain rate and temperature. An elevated dislocation density provided more activation energy for SRX, facilitating the recrystallization process and leading to a considerable decrease in the yield stress during phase II. Furthermore, an increased dislocation density accelerated the recrystallization process, causing phase III to initiate earlier with increasing prestrain. Figure 5c demonstrates the clear influence of the strain rate on the duration of the recovery phase I. Higher strain rates resulted in a shorter recovery phase, consequently leading to earlier recrystallization. Similarly, recrystallization (phase II) was completed earlier with an increasing strain rate, attributed to the elevated dislocation density, which serves as the driving force for the accelerated onset and termination of SRX [24]. As shown in Figure 5d, the initial yield stress after deformation was the highest for a prestrain of 0.8, followed by 0.01 and 0.1, with a difference of only 14 MPa between the highest and lowest values. Due to the sensitivity of the experimental setup, the yield stress dropped by varying degrees shortly after compression, as illustrated. Consequently, an evaluation of the onset of yield stress as a function of the strain rate is not provided.

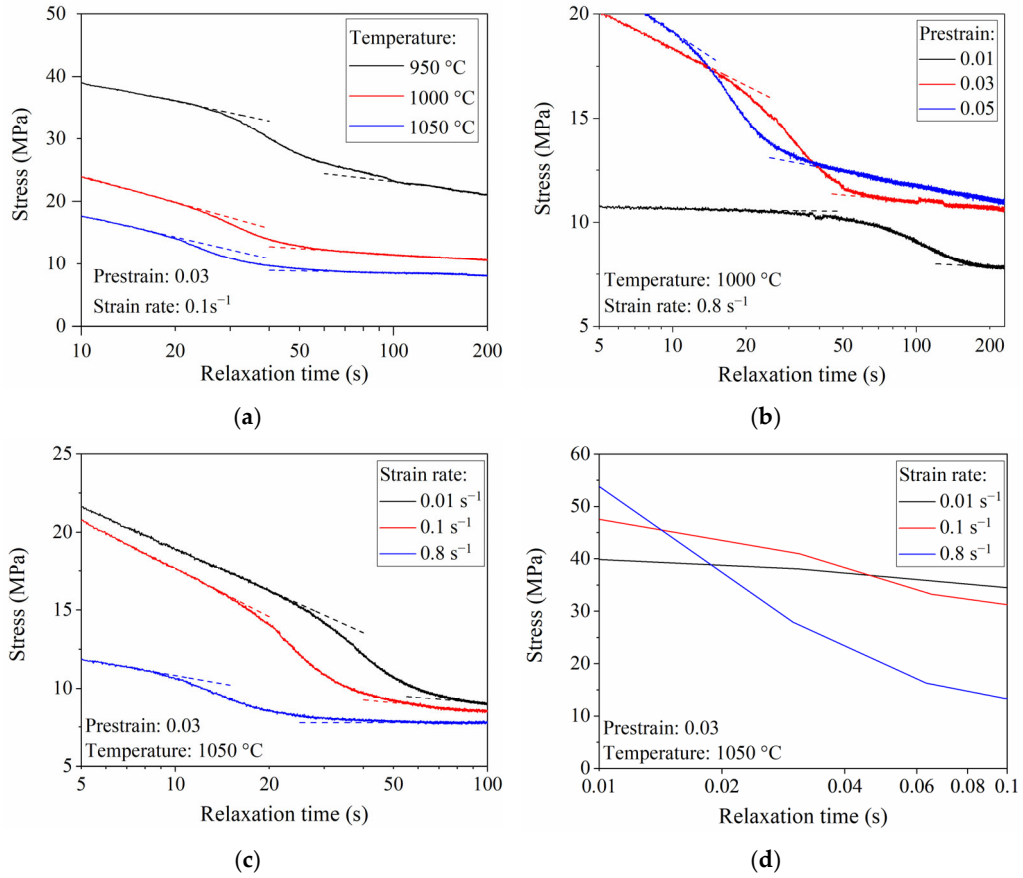

Figure 5. Stress relaxation curves of varying deformation conditions (**a**), varying temperatures, (**b**) varying prestrains, (**c**) varying strain rates, (**d**) onset of yield at varying strain rates.

3.2. Effect of Deformation States on SRX Behavior

Figure 6 presents the effects of varying deformation states on the volume fraction of SRX (X_{srx}) for 22MnB5, as calculated using Equation (1). The relaxation curves exhibit a typical sigmoidal slope, and the recrystallized fraction shows accelerated growth with rising relaxation time. The recrystallization process attained its maximum acceleration when 50% of the microstructure had undergone recrystallization. Subsequently, the rate of recrystallization gradually decreased until 100% of the microstructure was statically recrystallized. It is noteworthy that all curves exhibited an incubation time of several seconds, which is a characteristic behavior of SRX [13,15,16,19]. Remarkably, the recrystallization curves for 22MnB5 under various deformation conditions closely resemble the shape of an Avrami model.

Figure 6a illustrates the volumetric fraction curves of SRX for different deformation temperatures, employing a fixed strain rate of 0.1 s^{-1} and a prestrain of 0.03. The SRX fraction volume exhibits a discernible increment with the rise in deformation temperature from 950 °C to 1050 °C. This phenomenon is attributed to the thermally activated behavior of the recrystallization process, wherein higher temperatures facilitate an accelerated softening fraction. Consequently, the experimental steel subjected to 1050 °C demonstrates the earliest onset and completion of the SRX process, followed by 1000 °C and 950 °C. As a well-known characteristic, SRX is temperature-dependent due to its higher activation energy compared to metadynamic recrystallization (MDRX) [25]. Furthermore, Zahiri posited an additional consideration, involving the influence of the boron content in an IF steel [26]. At elevated temperatures, boron atoms exhibit enhanced mobility, thereby participating in the movement along the recrystallization front. In contrast, at lower temperatures, the segregation of boron atoms occurs at grain boundaries, impeding their mobility and consequently hindering the SRX process. The temperature-dependent SRX

behavior is comparable to that in reference [6,11], which was investigated for Mn-Si steel in a similar experimental range.

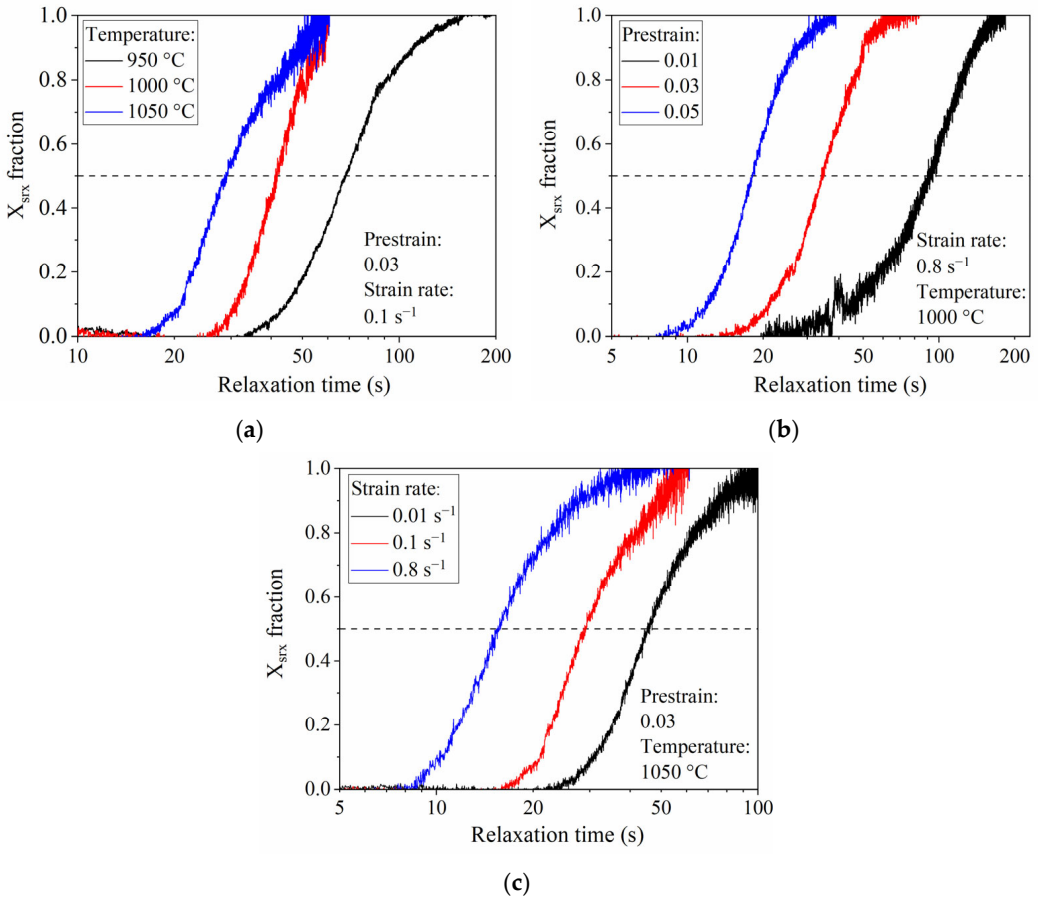

Figure 6. Softening curves of SRX fraction with varying deformation conditions: (**a**) varying temperature, (**b**) varying prestrain, (**c**) varying strain rate of 22MnB5.

Focusing on Figure 6b, the relaxation curves obtained from the tests conducted under three distinct prestrains (0.01, 0.03, and 0.05) and a strain rate of 0.8 s^{-1} at a constant deformation temperature of 1000 °C are displayed. These prestrains correspond to minor deformations intentionally maintained below the critical strain of the alloy, as elaborated in [27], resulting in a relatively low dislocation density. In contrast to MDRX, SRX exhibits pronounced sensitivity to the degree of prestrain, displaying an accelerated recrystallization process as the degree of prestrain increases [25].

Figure 6c showcases the SRX fraction volume curves at different strain rates, including 0.01 s^{-1}, 0.1 s^{-1}, and 0.8 s^{-1}, with a prestrain of 0.03 and a forming temperature of 1050 °C. Evidently, with an increase in the forming rate, the recrystallization process is likewise accelerated. Despite multiple increases in the strain rate starting from 0.01 s^{-1} up to 0.8 s^{-1}, the relaxation process experienced only a relatively minor shift to earlier times (from 20 s to 90 s at 0.01 s^{-1}, and from 8 s to 38 s at 0.8 s^{-1}). Among all the influencing forming parameters, the strain rate thus exhibited the weakest effect on SRX, which is consistent with the expected behavior for SRX [25]. Regarding similar steel grades, the significance of the process parameters can be determined analogously, with the strain rate appearing to have the least influence [18].

3.3. Modelling of SRX Kinetics of 22MnB5

3.3.1. Determination of $t_{0.5}$

For modeling SRX kinetics, it is necessary to determine the time for 50% recrystallization $t_{0.5}$. This is achieved by logarithm Equation (6), which results in the following equation:

$$lnt_{0.5} = lnT_{s1} + T_{s2}\, ln\, \varepsilon + T_{s3}\, ln\, \dot{\varepsilon} + \left(\frac{Q_{Ts}}{RT}\right) \tag{7}$$

With the help of a partial derivative of Equations (8)–(10), the material constants can be formulated as follows:

$$T_{s2} = \left.\frac{\partial lnt_{0.5}}{\partial ln\varepsilon}\right|_{\dot{\varepsilon},T=const.} \tag{8}$$

$$T_{s3} = \left.\frac{\partial lnt_{0.5}}{\partial ln\dot{\varepsilon}}\right|_{\varepsilon,T=const.} \tag{9}$$

$$Q_{Ts} = R\left.\frac{\partial lnt_{0.5}}{\partial (1/T)}\right|_{\varepsilon,\dot{\varepsilon}=const.} \tag{10}$$

The values of $t_{0.5}$ varying deformation states can be obtained from the experimental SRX curves, which are substituted into Equations (8)–(10). As shown in Figure 7a–c, the mean values for $T_{s2} = -0.8371$, $T_{s3} = -0.0515$, and $Q_{Ts} = 125.6050$ KJ/mol are calculated from the mean value of the slopes of $ln\ t_{0.5}$ versus $ln\ \varepsilon$, $ln\ t_{0.5}$ versus $ln\ \dot{\varepsilon}$ and $ln\ t_{0.5}$ versus $1/T$, respectively. Consequently, the value of T_{s1} can be derived from the intercept of ln $t_{0.5}$ versus $ln\varepsilon$ an average value of 3.1540×10^{-5}. Finally, Equation (11) for $t_{0.5}$ can be expressed as follows, where R represents the universal gas constant (8.314 J/mol·K), and T is the absolute temperature (K):

$$t_{0.5} = 3.1540 \times 10^{-5}\varepsilon^{-0.8371}\dot{\varepsilon}^{-0.0515} + \frac{125.6050}{RT} \tag{11}$$

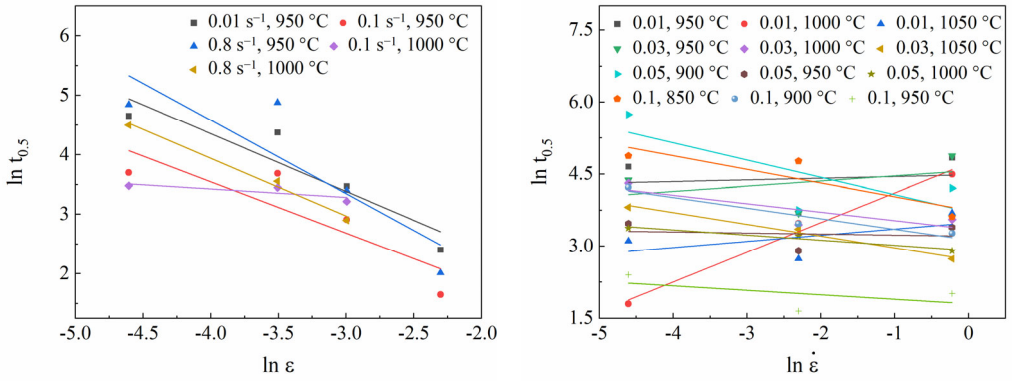

(**a**) (**b**)

Figure 7. *Cont.*

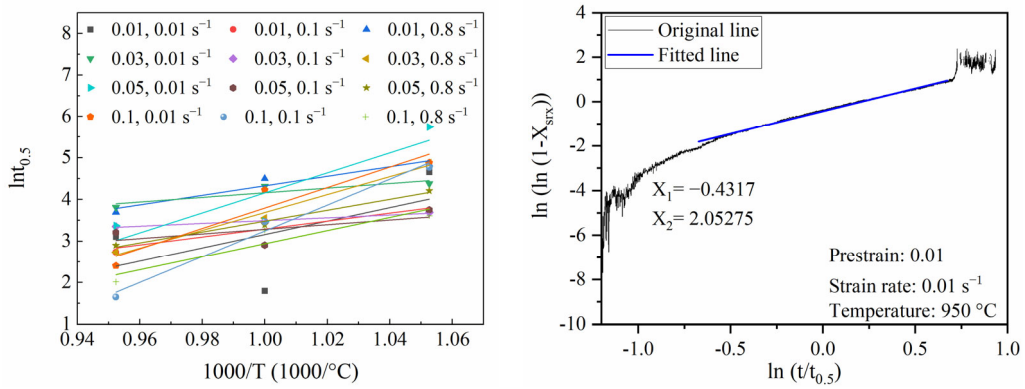

(**c**) (**d**)

Figure 7. Determination of material constants (**a**) T_{s2}, (**b**) T_{s3}, (**c**) Q_{Ts}, and (**d**) X_1 und X_2 of SRX kinetics for 22MnB5.

3.3.2. Determination of X_1 and X_2

The parameters X_1 and X_2 are calculated via the two-sided logarithmization of Equation (5), which leads to the following equation:

$$ln[ln(1-X)] = lnX_1 + X_2 ln\left(\frac{t}{t_{0.5}}\right) \quad (12)$$

By substituting the values for X and $t_{0.5}$ for different forming conditions of the Karjalainen [22] (see Equation (5)), the ratio of $ln[ln(1-X)]$ and $ln(t/t_{0.5})$ can be described. Consequently, the value for X_1 is -0.6659 and for X_2 the value is 2.3290, resulting in the following Avrami equation for SRX behavior:

$$X_{srx} = 1 - \exp[-0.6659\left(\frac{t}{t_{0.5}}\right)^{2.3290}] \quad (13)$$

3.4. Microstructural Evolution of 22MnB5 for SRX

3.4.1. Influence of Deformation on the Grain Size in SRX

Figure 8a–c presents the optically investigated microstructures of SRX in 22MnB5 boron–manganese steel subjected to a strain rate of 0.1 s^{-1} and a prestrain of 0.03, at deformation temperatures of 950 °C, 1000 °C, and 1050 °C, following stress relaxation tests. The micrographs reveal well-defined prior austenite grain (PAG) boundaries and exhibit a martensitic structure, discernible by the lath-like formations within the PAGs. While the PAGs exhibit globulitic characteristics, smaller individual grains are visible, albeit not to the extent typically observed in DRX [27]. The mean grain size of the PAGs was quantified using the lineal intercept method [20], resulting in average sizes of 32.3 µm for 950 °C, 33.6 µm for 1000 °C, and 37.0 µm for 1050 °C. Notably, the rise in the deformation temperature from 950 to 1050 °C predominantly influenced the grain growth behavior, leading to a slight increase in the average PAG size. The morphology of the grains and the grain size distribution is comparable to the statically recrystallized microstructure in similar steels and comparable experimental procedures [15,28].

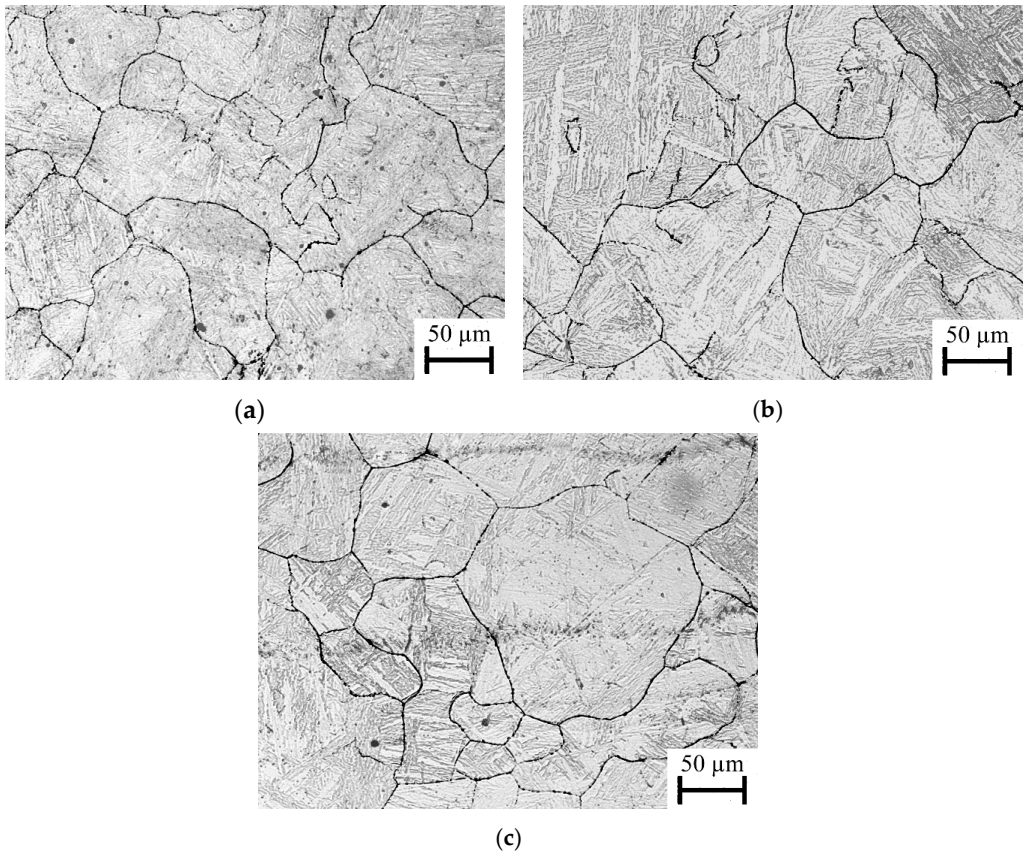

Figure 8. Optical investigated microstructures of SRX at a prestrain of 0.03, a strain rate 0.1 s^{-1}, and deformation temperatures of (**a**) 950 °C, (**b**) 1000 °C, (**c**) and 1050 °C after stress relaxation tests for 22MnB5 boron–manganese steel.

The influence of the strain rate on the optically investigated microstructure of SRX is depicted in Figure 9. Under a prestrain of 0.05 and a deformation temperature of 1000 °C, the mean sizes of the PAGs were measured as 37.0 µm, 32.8 µm, and 31.2 µm for the considered strain rates of 0.01 s^{-1}, 0.1 s^{-1}, and 0.8 s^{-1}, respectively. As previously mentioned, an increase in the strain rate provided a more significant driving force for grain refinement, resulting in observable effects in this case. The highest strain rate yielded the smallest grain size. The PAGs of the martensitic microstructure exhibited predominantly globulitic characteristics, and the presence of fine recrystallized grains was not readily discernible. This observation may be attributed to the prolonged holding times at elevated temperatures during the stress relaxation test. However, the fine lath structures of the martensitic microstructure are clearly distinguishable.

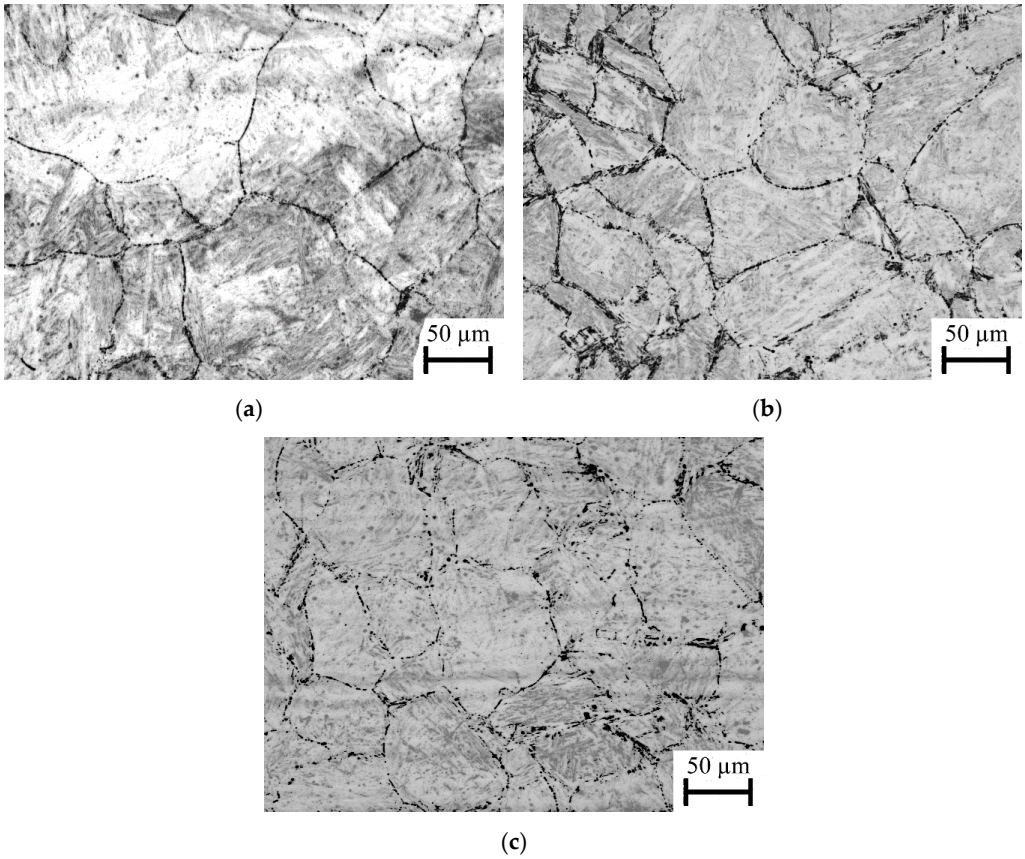

(**a**) (**b**)

(**c**)

Figure 9. Optical investigated microstructures of SRX at a prestrain of 0.05 and a deformation temperature of 1000 °C applied at strain rates of (**a**) 0.01 s^{-1}, (**b**) 0.1 s^{-1} and (**c**) 0.8 s^{-1} after stress relaxation tests for 22MnB5 boron–manganese steel.

The optically investigated microstructures of SRX, subjected to a deformation temperature of 1000 °C, a strain rate of 0.8 s^{-1}, and prestrains of 0.01, 0.03, and 0.05, are depicted in Figure 10a–c. Across all microstructural images, a prevailing martensitic microstructure with globulitic PAGs was observed. The mean grain sizes were determined as 32.8 µm, 37.7 µm, and 38.4 µm for the prestrains of 0.01, 0.03, and 0.05, respectively. The increase in grain size with the degree of deformation can be attributed to the following rationale: At a constant deformation temperature and a constant strain rate, an elevated prestrain promoted the kinetics of SRX. Consequently, under the conditions of a prestrain of 0.05, the completion of SRX occurred earlier compared to a prestrain of 0.01, allowing for an extended period of grain growth. Thus, for an equivalent duration, a larger prestrain corresponds to an increased amount of time for grain growth, ultimately resulting in an augmented mean size of the prior austenite grains, as evidenced by optical microscopy investigations.

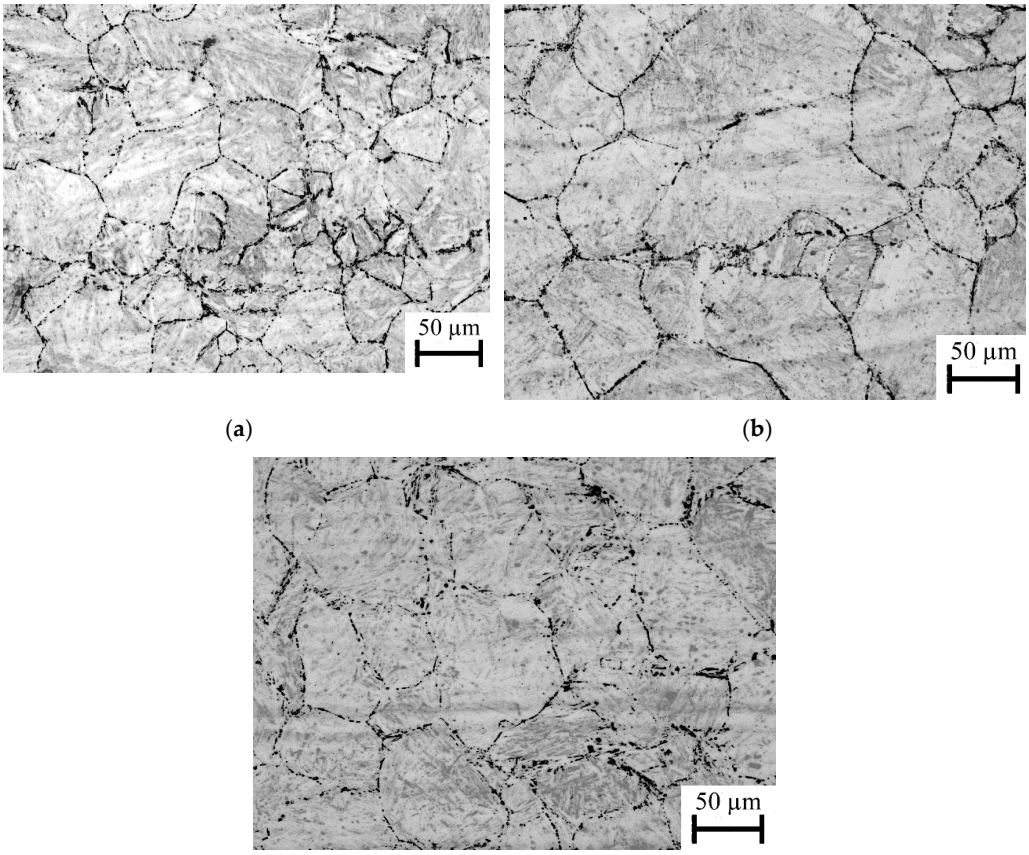

(**a**) (**b**)

(**c**)

Figure 10. Optical investigated microstructures of SRX at a strain rate of 0.8 s^{-1}, a deformation temperature of 1000 °C, and a prestrain of (**a**) 0.01, (**b**) 0.03, and (**c**) 0.05 after stress relaxation tests for 22MnB5 boron–manganese steel.

The SRX grain size primarily depends on the forming temperature and strain rate during the hot forming process, as can be seen in Figures 8–10. Therefore, the SRX grain size (D_{srx}) is modeled as a function of the forming temperature and strain rate [28,29].

$$D_{srx} = CZ^m \tag{14}$$

$$Z = \dot{\varepsilon} \exp\left(\frac{Q_{Ts}}{RT}\right) \tag{15}$$

The logarithm of both sides of Equation (14) produces the subsequent equation, where C and m denote the pertinent material constants governing the SRX kinetics, Z represents the Zener–Hollomon parameter, and Q_{Tm} signifies the activation energy specifically associated with SRX.

$$lnD_{srx} = ln\ C + m\ ln\ Z \tag{16}$$

By substituting different values of D_{srx} and Z, corresponding to various deformation conditions, into Equation (16), the interaction between the natural logarithms of Z and D_{srx} is revealed, as illustrated in Figure 11. Consequently, the values of C and m were precisely calculated as 45.2779 and −0.03198, respectively. This led to the formulation of the mathematical model describing the evolution of grain size resulting from SRX in 22MnB5 steel, expressed as:

$$D_{srx} = 45.2779\ Z^{-0.03198} \tag{17}$$

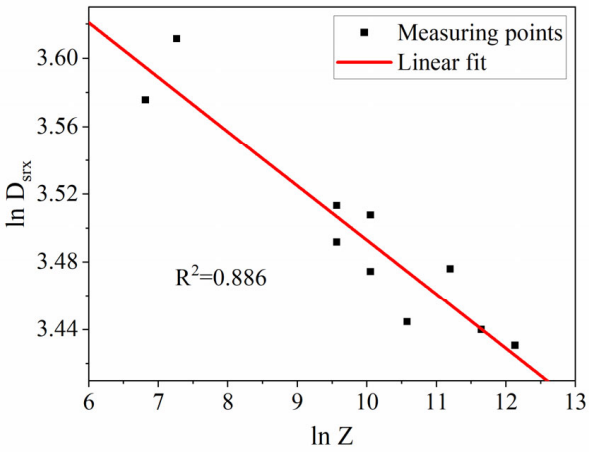

Figure 11. Relation of *ln Z* and *ln* D_{srx} for SRX of 22MnB5 steel.

3.4.2. Effect of SRX on Martensite Morphology

To replicate the rapid cooling rates observed in press-hardening processes, the specimens underwent high-pressure argon cooling after stress relaxation. The subsequent phase transformation resulted in a martensitic microstructure, originating from the former austenite phase, characterized by packets, blocks, and laths. Packets subdivide the PAGs into regions containing different laths, which share a common habit plane. These regions can be further divided into blocks, wherein the laths within a block are separated by low angles. It is worth noting that both the size of packets and blocks play pivotal roles in influencing the mechanical properties of low-carbon steels exhibiting a martensitic microstructure [30]. Due to their martensitic microstructure, it is not feasible to quantitatively analyze the recrystallized volume fraction using EBSD. This limitation arises because conventional criteria, like grain orientation spread (GOS) and mean grain misorientation (GAM), cannot be applied. Nonetheless, qualitative insights into the SRX process and the martensitic microstructure can still be gleaned. To examine the effects of temperature, prestrain, and strain rate on the microstructure following the stress relaxation test, EBSD measurements were conducted on the specimens under various deformation conditions, specifically with respect to the plastic strain, strain rate, and temperature: 0.03/0.01 s^{-1}/1000 °C, 0.03/0.01 s^{-1}/1050 °C, 0.03/0.8 s^{-1}/1050 °C, and 0.05/0.01 s^{-1}/1000 °C. To maintain consistency, it is worth noting that the same 300 s relaxation time was applied to all conditions, as illustrated in Figure 3. It should be mentioned that the holding time has a significant influence on both the grain size distribution and the average PAG size [31]. Representative sections for orientation mapping under different deformation conditions are displayed in Figure 12a–d. Employing the algorithm outlined by Nyyssönen et al. [21], calculations were performed to determine the prior austenite grain boundaries as well as the boundaries defining packets and blocks. The results are presented in Figure 12e–h, alongside corresponding band contrast figures.

The EBSD measurements reveal, for all analyzed samples, a fully martensitic microstructure. The PAGs (black lines) had an equiaxed morphology, and no strong orientation gradients were observed in the orientation mappings of the martensite. These points confirm the presence of a complete recrystallized austenitic microstructure before the quenching. After quenching, the microstructure of the samples consisted of lath martensite. Each PAG was composed of various packets (red lines), which were further subdivided into mostly parallel blocks (green lines). The lines delineate the regions of PAGs, packets, and blocks. Due to the spatial density in Figure 12, the areas of packets and blocks appear highly concentrated. For the deformation parameters of 0.03/0.01 s^{-1}/1000 °C (Figure 12a,e), 0.03/0.01 s^{-1}/1050 °C (Figure 12b,f) , and 0.05/0.01 s^{-1}/1000 °C (Figure 12d,h) , no significant difference in the PAG size could be determined. Also, the martensite packet and the block size show a similar size. This was to be expected, as the packet and block size correlated with the PAG size. It can be concluded that, for the investigated relaxation time of 300 s, the deformation temperature and the applied prestrain had no enhanced

influence on the feature size of the martensite. In contrast, an increase in the strain rate from 0.01 s^{-1} (Figure 12b,f) to 0.8 s^{-1} (Figure 12c,g) led to a clear decrease in the PAG size for the considered relaxation time. As a result, the size of the martensitic packets was decreased. Furthermore, for this sample, the density of the block boundaries seemed to be decreased. Larger areas without block boundaries are marked by white arrows in Figure 12g. A negative correlation between the packet and the block size was already reported by Shi et al. [30].

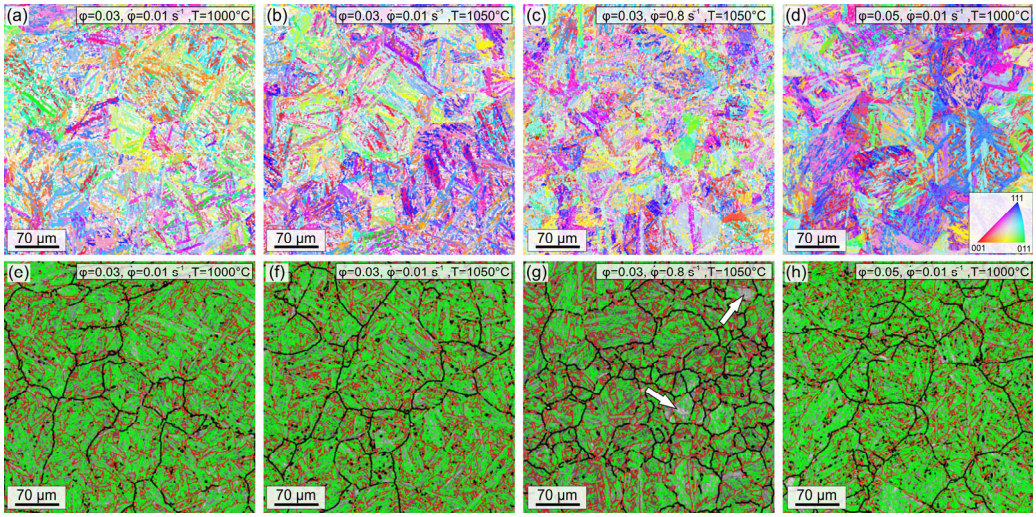

Figure 12. (**a**–**d**) EBSD orientation maps, utilizing IPF color coding relative to the sample surface, (**e**–**h**) EBSD band contrast maps that overlay reconstructed boundaries of the parent austenite grains (black lines), the packet boundaries (red lines), and block boundaries (green lines) within the martensitic structure. (**a**,**e**) 0.03, 0.01 s^{-1}, 1000 °C, (**b**,**f**) 0.03, 0.01 s^{-1}, 1050 °C, (**c**,**g**) 0.03, 0.8 s^{-1}, 1050 °C, (**d**,**h**) 0.05, 0.01 s^{-1}, 1000 °C.

4. Conclusions

In the present study, the SRX of 22MnB5 was investigated using a stress relaxation test after prior compression deformation in a temperature range between 950 °C and 1050 °C, with plastic strains of 0.01, 0.03, 0.05, and 0.1, and strain rates of 0.01 s^{-1}, 0.1 s^{-1}, and 0.8 s^{-1}, respectively. However, the parameter combinations must ensure that they do not exceed the temperature- and strain rate-dependent critical strain for DRX, according to [27], which means that not all combinations of the above parameters were used for determining static recrystallization. The following main conclusions are drawn from the results:

The stress relaxation tests exhibited a sigmoidal function in relation to time. The experimental parameters of temperature, prestrain, and strain rate influenced the transformation kinetics in descending order of magnitude. Regarding temperature, it was observed that an increase of 100 K reduced the transformation duration to a fraction. Similarly, the influence of prestrain resulted in a significant acceleration of the transformation kinetics with increasing prestrain. Confirming previous publications, it was reaffirmed that the strain rate had the least impact on SRX kinetics. Increasing the strain rate reduced the transformation duration, but the effect was marginal compared to the temperature and prestrain.

A constitutive model for SRX softening kinetics was developed based on an Avrami equation. The model's parameters confirm that the influence of prestrain was significantly higher than that of the strain rate.

Microstructural analyses using optical microscopy corroborate the results of the SRX model. However, the degree of microstructural change was not very pronounced. This may be attributed, among other factors, to the long holding time during the stress relaxation tests. It is expected that grain growth occurs in areas with early recrystallization, mitigating

differences. The grain size evolution was described using a model based on the Zener–Hollomon parameter.

The EBSD studies, similar to the optical microscopy observations, did not show a significant alteration in the grain boundary misorientation of individual grains. However, samples subjected to high deformation rates exhibited smaller grain sizes, and the density of block boundaries seemed to be decreased.

Practical implications regarding the SRX can be stated as follows. In industrial processes, it may be beneficial to deliberately increase the process temperature and deformation speed to achieve a defined grain refinement. This can lead to an improvement in the strength and ductility of the component due to the Hall–Patch effect. Furthermore, there is the possibility of integrating the models into FE software to predict grain size development and recrystallized fractions resulting from static recrystallization (SRX).

The limitations of the chosen research approach are as follows. The stress relaxation test offers significant advantages by use of the double compression test, as described above. However, signal noise negatively affects the quality of results, as evident in the sigmoidal curves. Additionally, with slow SRX and under consideration of the sigmoidal curve pattern, it can be challenging to determine the point of recrystallization completion accurately. Therefore, precise analysis of the microstructure, especially regarding the packets and blocks, is difficult without representing the grain growth effects. Moreover, SRX requires staying below the critical strain. The plastic strain, and consequently, the measured forces, are relatively low, making errors in the experimental and measurement setups more significant.

Author Contributions: Conceptualization, P.B. and S.P.; methodology, P.B.; investigation, P.B., S.P. and K.N.; writing—original draft preparation, P.B. and S.P.; writing—review and editing, A.K.; visualization, P.B. and S.P.; supervision, A.K.; project administration, P.B. and A.K. All authors have read and agreed to the published version of the manuscript.

Funding: The authors would like to gratefully acknowledge the financial support by the Deutsche Forschungsgemeinschaft (DFG, German Research Foundation) project number 491.193.532, and the Chemnitz University of Technology.

Data Availability Statement: The data that support the findings of this study are available from the corresponding author, P.B., upon reasonable request.

Conflicts of Interest: The authors declare no conflict of interest.

References

1. Singh, A.K.; Narasimhan, K. Effect of strain rate on formability of 22MnB5 steel during hot stamping process. *IOP Conf.* **2021**, *1157*, 012022. [CrossRef]
2. Wróbel, I.; Skowronek, A.; Grajcar, A. A Review on Hot Stamping of Advanced High-Strength Steels: Technological-Metallurgical Aspects and Numerical Simulation. *Symmetry* **2022**, *14*, 969. [CrossRef]
3. Zhao, B.; Chiriac, C.; Daun, K.J. Evaluation of 22MnB5 Steel Austenitization Sub-Models for Simulating the Heating Phase of Hot Stamping. *IOP Conf.* **2020**, *967*, 012076. [CrossRef]
4. Çavuşoğlu, O.; Çavuşoğlu, O.; Yılmazoğlu, A.G.; Üzel, U.; Aydın, H.; Güral, A. Microstructural features and mechanical properties of 22MnB5 hot stamping steel in different heat treatment conditions. *J. Mater. Res. Technol.* **2020**, *9*, 10901–10908. [CrossRef]
5. Palmieri, M.E.; Galetta, F.R.; Tricarico, L. Study of Tailored Hot Stamping Process on Advanced High-Strength Steels. *J. Manuf. Mater. Process.* **2022**, *6*, 11. [CrossRef]
6. Somani, M.C.; Porter, D.A.; Karjalainen, L.P.; Kantanen, P.K.; Kömi, J.I.; Misra, D.K. Static recrystallization characteristics and kinetics of high-silicon steels for direct quenching and partitioning. *Int. J. Mater. Res.* **2019**, *110*, 183–193. [CrossRef]
7. Miura, H.; Kobayashi, M.; Watanabe, C.; Sugiura, N.; Yoshinaga, N. Static recrystallization behavior and mechanical properties of heterogeneous nanostructured duplex phase stainless steel. *Mater. Trans.* **2020**, *61*, 416–419. [CrossRef]
8. Hodgson, P.D. A mathematical model to predict the mechanical properties of hot rolled C-Mn and microalloyed steels. *ISIJ Int.* **1992**, *32*, 1329–1338. [CrossRef]
9. Salehi, M.S.; Serajzadeh, S. A neural network model for prediction of static recrystallization kinetics under non-isothermal conditions. *Comput. Mater. Sci.* **2010**, *49*, 773–781. [CrossRef]

10. Shen, W.; Zhang, C.; Zhang, L.; Xu, Q.; Cui, Y.; Xu, Y. A modified Avrami equation for kinetics of static recrystallization of Nb-V microalloyed steel: Experiments and numerical simulation. *Vacuum* **2018**, *150*, 116–123. [CrossRef]
11. Fernández, A.I.; Uranga, P.; López, B.; Rodriguez-Ibabe, J.M. Static recrystallization behaviour of a wide range of austenite grain sizes in microalloyed steels. *ISIJ Int.* **2020**, *40*, 893–901. [CrossRef]
12. Bo, M.A.; Yan, P.; Bin, J.; Liu, Y.F. Static recrystallization kinetics model after hot deformation of low-alloy steel Q345B. *J. Iron Steel Res. Int.* **2010**, *17*, 61–66.
13. Zhao, M.; Huang, L.; Zeng, R.; Wen, D.; Su, H.; Li, J. In-situ observations and modeling of static recrystallization in 300 M steel. *Mater. Sci. Eng. A* **2019**, *765*, 138300. [CrossRef]
14. Luo, M.; Zhou, B.; Li, R.B.; Xu, C.; Guo, Y.H. Static recrystallization behavior of $Z_{12}CN_{13}$ martensite stainless steel. *J. Mater. Eng. Perform.* **2017**, *26*, 4157–4165. [CrossRef]
15. Wang, X.H.; Liu, Z.B.; Liang, J.X.; Yang, Z.Y.; Sun, Y.Q.; Wang, C.J.; Qi, Y. A study on the static recrystallization behavior of an ultrahigh-strength stainless steel. *Mater. Res. Express* **2021**, *8*, 056504. [CrossRef]
16. Kaikkonen, P.M.; Somani, M.C.; Karjalainen, L.P.; Kömi, J.I. Flow stress behaviour and static recrystallization characteristics of hot deformed austenite in microalloyed medium-carbon bainitic steels. *Metals* **2021**, *11*, 138. [CrossRef]
17. Zhang, Q.; Huo, X.; Li, L.; Chen, S.; Lu, C. Correlation between Precipitation and Recrystallisation during Stress Relaxation in Titanium Microalloyed Steel. *Metals* **2022**, *12*, 1920. [CrossRef]
18. Facusseh, C.; Salinas, A.; Flores, A.; Altamirano, G. Study of Static Recrystallization Kinetics and the Evolution of Austenite Grain Size by Dynamic Recrystallization Refinement of a Eutectoid Steel. *Metals* **2019**, *9*, 1289. [CrossRef]
19. Vervynckt, S.; Verbeken, K.; Thibaux, P.; Houbaert, Y. Characterization of the Austenite Recrystallization by Comparing Double Deformation and Stress Relaxation Tests. *Steel Res. Int.* **2010**, *81*, 234–244. [CrossRef]
20. *ASTM E112-96*; Standard Test Methods for Determining Average Grain Size. ASTM International: West Conshohocken, PA, USA, 2004.
21. Nyyssönen, T.; Isakov, M.; Peura, P.; Kuokkala, V.T. Iterative Determination of the Orientation Relationship between Austenite and Martensite from a Large Amount of Grain Pair Misorientations. *Metall. Mater. Trans. A* **2016**, *47*, 2587–2590. [CrossRef]
22. Karjalainen, L.P. Stress Relaxation Method for Investigation of Softening Kinetics in Hot Deformed Steels. *Mater. Sci. Technol.* **1995**, *11*, 557–565. [CrossRef]
23. Perttula, J.; Karjalainen, L.P. Recrystallisation rates in austenite measured by double compression and stress relaxation methods. *Mater. Sci. Technol.* **1998**, *14*, 626–630. [CrossRef]
24. Laasraoui, A.; Jonas, J.J. Recrystallization of austenite after deformation at high temperatures and strain rates—Analysis and modeling. *Metall. Trans. A* **1991**, *22*, 151–160. [CrossRef]
25. Jonas, J.; Poliak, E.; Najafizadeh, A. The Strain Dependence of Post-Deformation Softening during the Hot Compression of 304H Stainless Steel. *Mater. Sci. Forum* **2007**, *100–107*, 539–543.
26. Zahiri, S.; Byon, S.; Kim, S.; Lee, Y.; Hodgson, P. Static and metadynamic recrystallization of interstitial free steels during hot deformation. *ISIJ Int.* **2004**, *44*, 1918–1923. [CrossRef]
27. Xu, Y.; Birnbaum, P.; Pilz, S.; Zhuang, X.; Zhao, Z.; Kräusel, V. Investigation of constitutive relationship and dynamic recrystallization behavior of 22MnB5 during hot deformation. *Results Phys.* **2019**, *14*, 102426. [CrossRef]
28. Lin, Y.C.; Chen, M.S. Study of Microstructural Evolution during Static Recrystallization in a Low Alloy Steel. *J. Mater. Sci.* **2009**, *44*, 835–842. [CrossRef]
29. Choi, S.; Lee, Y. A New Approach to Predicting Partial Recrystallization in the Multi-Pass Hot Rolling Process. *Met. Mater. Int.* **2002**, *8*, 15–23. [CrossRef]
30. Shi, Z.; Liu, K.; Wang, M.; Shi, J.; Dong, H.; Pu, J.; Chi, B.; Zhang, Y.; Jian, L. Effect of Tensile Deformation of Austenite on the Morphology and Strength of Lath Martensite. *Met. Mater. Int.* **2012**, *18*, 317–320. [CrossRef]
31. Ali, M.; Seppälä, O.; Fabritius, T.; Kömi, J. Microstructure evolution and static recrystallization kinetics in hot-deformed austenite of coarse-grained Mo-free and Mo containing low-carbon CrNiMnB ultrahigh-strength steels. *Mater. Today Commun.* **2022**, *33*, 104676. [CrossRef]